Supporting Information for "Geodynamic Modeling with Uncertain Initial Geometries"

A. Spang [1], T. S. Baumann [1], B. J. P. Kaus [1,2]

[1]Johannes Gutenberg University, Institute of Geosciences, Johann-Joachim-Becher-Weg 21, 55128 Mainz, Germany

[2]TeMaS, Terrestrial Magmatic Systems Research Center, temas.uni-mainz.de

Contents of this file:

Corresponding author: A. Spang, Department of Geosciences, Johannes Gutenberg University, Johann-Joachim-Becher-Weg 21, 55128 Mainz, Germany. (arspang@uni-mainz.de)

June 10, 2022, 4:40pm

Introduction

This file contains supplementary texts about methodology (S1: General workflow, S2: Additional Options, S3: Model Details), results (S4: Asymmetry) and a simple inversion example for the subduction application (S5: Inverting for Initial Angle). Furthermore, it contains the supplementary Figures S1 to S5 associated with methodology, Figures S6 to S9 associated with Application I: Salt, Figure S10 associated with Application II: Subduction and Figure S11 associated with text S5. Finally, supplementary tables S1 and S2 containing the material parameters used and table S3 containing scaling parameters used in Application I: Salt.

Text S1: General workflow

This text outlines the general workflow of how our tool can be used for a geodynamic study. It contains 7 steps (illustrated in Figure S1), of which the last 4 may repeat if an inversion is to be performed. Steps 1-4, 6 and 7 can be completed on any modern computer or laptop that has access to Inkscape, Matlab and Paraview (for visualization only). Step 5 requires LaMEM and more computing power. Single 2D simulations can be performed on regular machines but for 3D or a large number of 2D simulations, a computing cluster is necessary.

(i) Draw the reference geometry in Inkscape. This includes all units like the background lithosphere, mantle and anomalous bodies like salt and magma bodies or subducting plates. Instructions can be found at: https://bitbucket.org/geomio/geomio/wiki/Home. This results in an .svg file.

(ii) Use the basic functionality of geomIO to read the .svg file and create the reference geometry. This results in a .vtk file for each unit. The different units can be visualized directly in Matlab. Alternatively, the .vtk files can be opened in Paraview.

(iii) Choose the unit that should be varied and the control polygons. Prepare and load in scaling parameters for each variation or use the build-in options to generate them.

(iv) Use the new functionality of geomIO and the options selected in step (iii) to create an ensemble of setups. Figure S2 shows examples of how this can be accomplished. For a more detailed description of all available options visit https://bitbucket.org/geomio/geomio/wiki/VaryGeomTutorial.md.

(v) Use LaMEM to run forward models with each of the setups generated in step (iv).

(vi) Use any software to post-process the results from LaMEM (e.g. compute a misfit to observations, analyze result dependencies on input parameters). LaMEM output is in .vtk format, so it can be directly visualized in Paraview, or read and reformatted in Python or Julia.

(vii) Optional: Select new scaling parameters and return to step (iv). New scaling parameters can be the result of an optimization algorithm (e.g., neighborhood algorithm (Sambridge, 1999), NAplus (Baumann et al., 2014)).

To reproduce the results (including Figures) of this study, visit our repository on zenodo (https://doi.org/10.5281/zenodo.6538270). It contains the versions of geomIO and LaMEM that were utilized as well as detailed step-by-step instructions of how to reproduce our results. As LaMEM requires more computing power, we also included the post-processed output in the repository.

Text S2: Additional Options

Text S2.1: Absolute Transformation Parameters

One issue of the method described in section 2.1.3 is that the absolute change in coordinates of polygon nodes is determined by the size of the polygon. In Figure S3b, the central polygon (lowermost control polygon) is elongated by 0.5 units in y-direction while the lowermost polygon is only elongated by 0.015 units. If this effect is not desired, we offer a second transformation algorithm which works with absolute transformation parameters (dx and dy). dx and dy are the maximum transformations per direction and they are scaled for every node on the polygon, depending on the node's position:

$$\left(\vec{x}_{new} \;\; \vec{y}_{new}\right) = \left(\vec{x} \;\; \vec{y}\right) + \left(\frac{\vec{x}'}{|\overrightarrow{xy}|} \;\; \frac{\vec{y}'}{|\overrightarrow{xy}|}\right) * \begin{pmatrix} dx & 0 \\ 0 & dy \end{pmatrix} \tag{S1}$$

$$|\overrightarrow{xy}|_n = \sqrt{{x'_n}^2 + {y'_n}^2} \tag{S2}$$

The fraction in equation S1 corresponds to element-wise division. The lower half of the body in Figure S3c was changed with absolute transformation parameters. While the central polygon (lowermost control polygon) is identical to the one in Figure S3b, all polygons below are wider, most notably the lowest one. Figure S4a shows how the different methods affect the lowermost polygon. The approach of absolute transformation is limited when it comes to shrinking parts of the body which have very small polygons.

Text S2.2: Coordinate rotation

The body might have a preferred orientation which is not aligned with either the x- or the y-direction, so scaling it in a different direction might be desirable. To do that, we include the option to rotate the coordinate system such that the orientation, in which transformation is preferred, aligns with one of the axes. This is done by defining the rotation matrix

$$Q = \begin{pmatrix} cos(\theta) & sin(\theta) \\ -sin(\theta) & cos(\theta) \end{pmatrix} \tag{S3}$$

where θ represents the preferred direction of transformation and rotates the coordinate system clockwise. To apply it, equation 3 has to be modified to:

$$\begin{pmatrix} \vec{x}_{i,new} & \vec{y}_{i,new} \end{pmatrix} = \begin{pmatrix} \vec{x_i}' & \vec{y_i}' \end{pmatrix} * Q * \begin{pmatrix} Sx_1 & 0 \\ 0 & Sy_1 \end{pmatrix} * Q^T + \begin{pmatrix} x_{i_c} & y_{i_c} \\ ... & \\ x_{i_c} & y_{i_c} \end{pmatrix} \tag{S4}$$

Figure S4b shows an example case where a polygon is elongated in NNE-SSW direction, so without rotating the coordinate system it would not be possible to only transform the polygon along its longest axis. However, by rotating the y-axis to align with the orientation, then applying the scaling and rotating it back, we can do that. Figure S4c shows that more complex shapes can be handled in the same way.

Text S3.1: LaMEM

For our models, we utilize the thermomechanical finite differences code LaMEM (Kaus et al., 2016). It solves for the conservation of momentum, mass and energy (eq. S5-S7), using a staggered grid in combination with a marker-in-cell approach (Harlow & Welch, 1965).

$$\frac{\partial \tau_{ij}}{\partial x_j} - \frac{\partial p}{\partial x_i} + \rho g_i = 0 \tag{S5}$$

$$\frac{1}{K}\frac{Dp}{Dt} - \alpha \frac{DT}{Dt} + \frac{\partial v_i}{\partial x_i} = 0 \tag{S6}$$

$$\rho C_p \frac{DT}{Dt} = \frac{\partial}{\partial x_i}\left(\lambda \frac{\partial T}{\partial x_i}\right) \tag{S7}$$

τ_{ij} is the Cauchy stress deviator, $x_i (i = 1, 2, 3)$ denotes the Cartesian coordinates, p is pressure (positive in compression), ρ density, g_i gravitational acceleration, K the bulk modulus, α the thermal expansion coefficient, T the temperature, v_i the velocity vector, C_p the specific heat capacity, λ the thermal conductivity and D/Dt is the material time derivative.

The rocks are characterized by a visco-elasto-plastic rheology where the strain rate is the sum of the elastic, viscous and plastic components:

$$\dot{\epsilon}_{ij} = \dot{\epsilon}^{el}_{ij} + \dot{\epsilon}^{vi}_{ij} + \dot{\epsilon}^{pl}_{ij} \tag{S8}$$

$\dot{\epsilon}_{ij}$ denotes the total deviatoric strain rate tensor, while $\dot{\epsilon}^{el}_{ij}$, $\dot{\epsilon}^{vi}_{ij}$ and $\dot{\epsilon}^{pl}_{ij}$ represent the elastic, viscous and plastic strain rate components. For a detailed discussion of this equation and all of its components, the reader is referred to Kaus et al. (2016). Here we will focus on the material parameters which impact the 3 components.

The elastic component depends on the shear modulus G:

$$\dot{\epsilon}_{ij}^{el} = \frac{1}{2G}\frac{D\tau_{ij}}{Dt}, \tag{S9}$$

where $D\tau_{ij}/Dt$ is the objective derivative of the stress tensor.

The viscous component depends on the viscosity η:

$$\dot{\epsilon}_{ij}^{vi} = \frac{\tau_{ij}}{2\eta} \tag{S10}$$

η is either a constant (see tables S1 and S2) or follows the stress- and temperature-dependent powerlaw relationship of dislocation creep:

$$\eta = \frac{1}{2}(B_n)^{-\frac{1}{n}}(\dot{\epsilon}_{II})^{\frac{1}{n}-1}\exp\left(\frac{E_n + pV_n}{nRT}\right), \tag{S11}$$

where B_n is the creep constant, $\dot{\epsilon}_{II}$ the square root of the second invariant of the strain rate ($\dot{\epsilon}_{II} = (\frac{1}{2}\dot{\epsilon}_{ij}\dot{\epsilon}_{ij})^{1/2}$), E_n the activation energy, p the pressure, V_n the activation volume, n the powerlaw exponent, R the universal gas constant and T the temperature.

The plastic component is governed by the Drucker-Prager failure criterion (Drucker & Prager, 1952):

$$\tau_{II} \leq \sin(\phi)p + \cos(\phi)c_0 \tag{S12}$$

where τ_{II} is the square root of the second invariant of the stress tensor ($\tau_{II} = (\frac{1}{2}\tau_{ij}\tau_{ij})^{1/2}$), ϕ is the friction angle, p the pressure and c_0 the cohesion. As long as τ_{II} does not exceed the failure criterion, the stress is accommodated by visco-elastic deformation.

Text S3.2: Model Details Application I: Salt

We model a homogeneous slice of crust that is 20 km wide and deep and hosts a 3.5 km thick salt bed from which the diapir rises. Along the boundaries of the model, we employ free slip conditions (velocities normal to boundaries equal zero). At the top of the crust, we use a stabilized (Kaus et al., 2010) stress free internal surface and 5 km thick layer of sticky air (Crameri et al., 2012). We use 128 cells in the horizontal and 256 cells in vertical direction. For simplicity, we use linear viscosities η for all materials. Table S1 summarizes the material parameters that we employed. A shear modulus of 15 GPa and a Poisson's ratio of 0.25 correspond to a Young's modulus of 37.5 GPa which is consistent with previous laboratory and modeling studies on salt (Ingraham et al., 2015, June; Zong et al., 2017; Baumann et al., 2018).

Text S3.3: Model Details Application II: Subduction

Our subduction model is 2000 km wide and extends from the surface to 660 km depth. We use 512 cells in the horizontal and 256 cells in the vertical direction, yielding resolutions of about 4 and 2.5 km respectively. The 100 km thick continent is made up of 40 km of crust and 60 km of lithospheric mantle. We assign different linear temperature gradients to the continental crust and lithosphere and use a half-space cooling model for the subducting plate that corresponds to a thermal age of 30 Myr. As the plate has already started subducting at the start of our simulations, we add another 1 Myr of temperature diffusion to account for the heating during that initial stage of subduction (Figure S10a). All materials are described by a temperature- and stress-dependent visco-plastic rheology. Table S2 summarizes all material parameters. We use free slip boundary conditions along all model edges and do not prescribe any boundary velocities.

Text S4: Asymmetry

The asymmetry was introduced by slightly reducing the curvature of the diapir head on one side (Figure 3, S8). As for the symmetric case, we can see a clear distinction between faults that develop from the center of the diapir head and those that develop from the side of the head (Figure S8a,d). But while central faults still develop to both sides, outside faults now exclusively develop on one side of the diapir (Figure S8c,f). Mirroring the asymmetry leads to a mirrored result. In all cases, outside faults now appear on the side that retained the original curvature.

This suggests that for symmetric cases, the side that develops the dominant fault is influenced by the small difference between how one side of the curved diapir boundary aligns with the grid cells compared to the other side. This is still the case for the central faults at asymmetric diapirs, but towards the outside of the diapir head, the asymmetry is more important for the location of the dominant fault.

Text S5: Inverting for Initial Angle

Reconstructions (e.g. Sdrolias & Müller, 2006) show that convergence velocities between plates fluctuate throughout the evolution of subduction zones. These fluctuations are frequently interpreted to be the result of subdcution of ocean plateaus or ridges (e.g. Martinod et al., 2010) but our models show that the convergence rate also fluctuates without any changes in the elevation or density structure of the oceanic plate. Instead the velocity profile seems to be coupled to the initial dip of the subducting slab (β_0), so given a good understanding of the rheology of the system, a velocity reconstruction could also be used to invert for an initial angle using modeling. To demonstrate the feasibility of this approach, we use a synthetic profile that we generated using $\beta_0 = 72.5°$ (dotted line in Figure S11a). We add normally distributed random noise ($\sigma = 0.5\,\mathrm{cm\,yr^{-1}}$) to the profile to get a synthetic observation in 1 Myr intervals (black circles in Figure S11a). We then run a set of models in 5° intervals (blue in Figure S11b), compute the RMS misfit (Φ) and add models in 1° intervals in areas of low misfit (orange in Figure S11b).

Figure S11b shows that we can find the true β_0 with only a few forward models. In a real application, there might be more parameters involved in the inversion process but as there is an obvious dependency of the velocity profile on the initial angle, an inversion with more models should still converge to the correct solution.

References

Baumann, T. S., Kaus, B., & Popov, A. A. (2018). Deformation and stresses related to the gorleben salt structure: insights from 3d numerical models. *Mechanical Behavior of Salt, Saltmech IX*, 15–27.

Baumann, T. S., Kaus, B. J. P., & Popov, A. A. (2014). Constraining effective rheology through parallel joint geodynamic inversion. *Tectonophysics*, *631*, 197–211. doi: https://doi.org/10.1016/j.tecto.2014.04.037

Crameri, F., Schmeling, H., Golabek, G. J., Duretz, T., Orendt, R., Buiter, S., ... Tackley, P. (2012). A comparison of numerical surface topography calculations in geodynamic modelling: an evaluation of the 'sticky air'method. *Geophysical Journal International*, *189*(1), 38–54.

Drucker, D. C., & Prager, W. (1952). Soil mechanics and plastic analysis or limit design. *Quarterly of applied mathematics*, *10*(2), 157–165.

Harlow, F. H., & Welch, J. E. (1965). Numerical calculation of time-dependent viscous incompressible flow of fluid with free surface. *The physics of fluids*, *8*(12), 2182–2189.

Ingraham, M. D., Broome, S. T., Bauer, S. J., Barrow, P. C., & Flint, G. M. (2015, June). Behavior of salt from the bayou choctaw salt dome. In *49th US Rock Mechanics/Geomechanics Symposium.*

Kaus, B. J. P., Mühlhaus, H., & May, D. A. (2010). A stabilization algorithm for geodynamic numerical simulations with a free surface. *Physics of the Earth and Planetary Interiors*, *181*(1-2), 12–20.

Kaus, B. J. P., Popov, A. A., Baumann, T., Pusok, A., Bauville, A., Fernandez, N., & Collignon, M. (2016). Forward and inverse modelling of lithospheric deformation on

geological timescales. In *Proceedings of NIC Symposium.*

Martinod, J., Husson, L., Roperch, P., Guillaume, B., & Espurt, N. (2010). Horizontal subduction zones, convergence velocity and the building of the Andes. *Earth and Planetary Science Letters*, *299*(3-4), 299–309.

Sambridge, M. (1999). Geophysical inversion with a neighbourhood algorithm-I. Searching a parameter space. *Geophysical Journal International*, *138*(2), 479-494. doi: 10.1046/j.1365-246X.1999.00876.x

Sdrolias, M., & Müller, R. D. (2006). Controls on back-arc basin formation. *Geochemistry, Geophysics, Geosystems*, *7*(4).

Zong, J., Stewart, R. R., Dyaur, N., & Myers, M. T. (2017). Elastic properties of rock salt: Laboratory measurements and gulf of mexico well-log analysis. *Geophysics*, *82*(5), D303–D317.

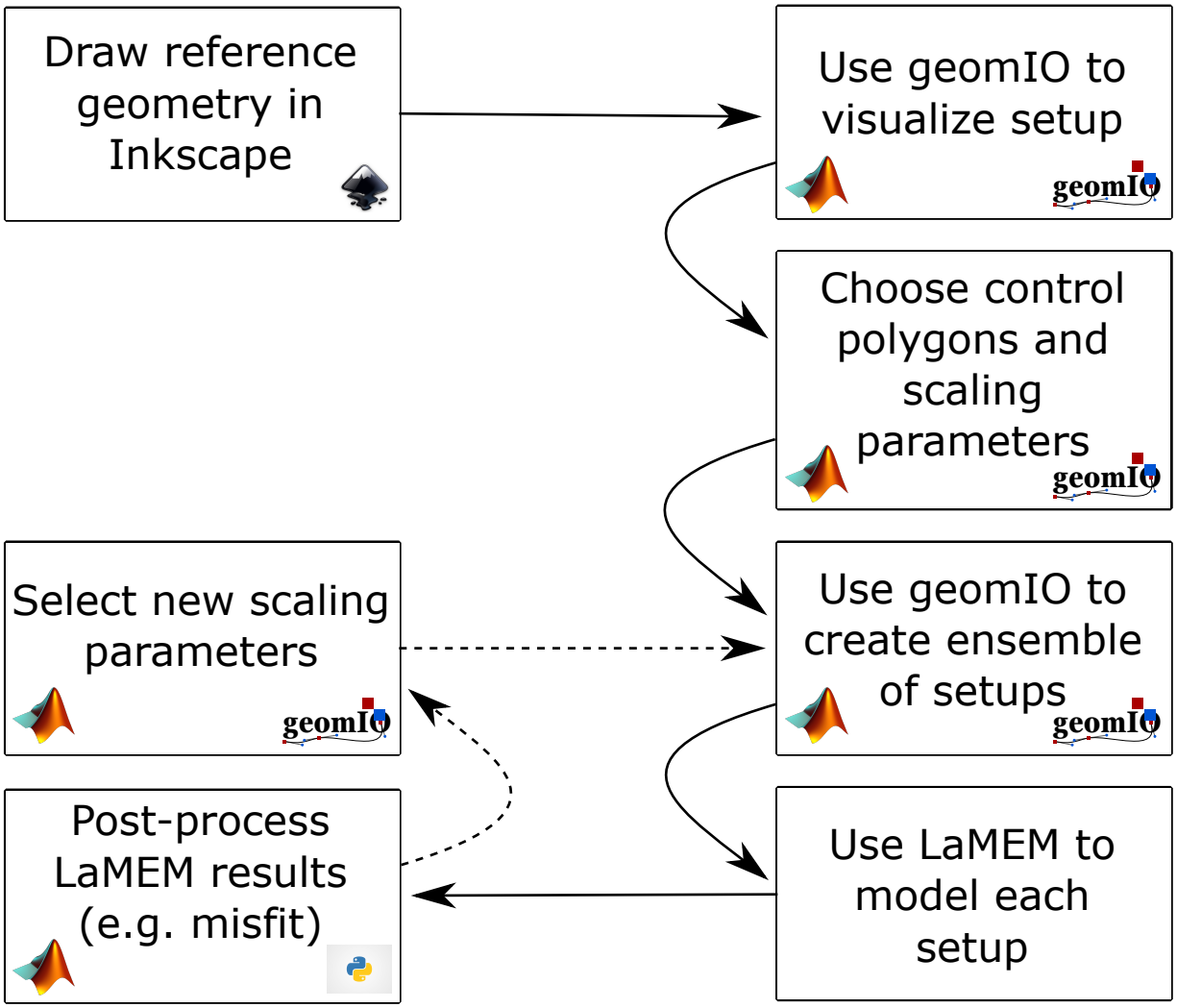

Figure S1. General workflow for using geomIO and the new tool presented in this work in combination with LaMEM. The dashed arrows indicate that these steps are optional and are only necessary to minimize misfit or explore additional parameter space. Text S1 describes the procedure in more detail.

(a)

```
% vary geom settings
opt.varyGeom.do             = true;                 % activate geometry vatriation
opt.varyGeom.volume         = 'Diapir';             % name of volume in Inkscape
opt.varyGeom.dim            = '2D_X';               % mode
opt.varyGeom.genType        = 'grid';               % how to generate scaling parameters
opt.varyGeom.Grid.lb        = [0.5; 0.5; 0.5; 0.5]; % lower bound for scaling parameter generation
opt.varyGeom.Grid.ub        = [2.0; 3.0; 2.0; 1.5]; % upper bound for scaling parameter generation
opt.varyGeom.Grid.num       = [2; 2; 2; 2];         % number of samples for each scaling parameter
opt.varyGeom.Grid.Sz        = [0.8; 1.1; 2];        % options for vertical scaling parameter generation
opt.varyGeom.Grid.noise     = 0.3;                  % noise to be added to scaling parameters
opt.varyGeom.stretchType    = 'factor';             % scale by factor or absolute value
opt.varyGeom.SzType         = 'bot';                % reference level for vertical stretching
opt.varyGeom.CtrlPoly       = [153, 253, 385, 482]; % indices of control polygons
opt.varyGeom.CP_ref         = 'global';             % reference system for control polygons
opt.varyGeom.CP_track       = true;                 % control polygons cahnge depth with vertical scaling
opt.varyGeom.outName        = './SaltExample';      % output name
opt.varyGeom.outNameOffset  = 0;                    % offset numbering of output
opt.varyGeom.writeParaview  = false;                % write .vtk files
opt.varyGeom.writePolygons  = true;                 % write LaMEM polygons
opt.varyGeom.drawOutlines   = true;                 % draw outline along profile
opt.varyGeom.outlineProf    = [0, 0];               % coordinates of outline profile
```

(b)

```
% vary subduction settings
opt.varySub.do           = true;         % activate subduction variation
opt.varySub.vols         = 'SimpleSlab'; % name of volume in Inkscape
opt.varySub.ref          = 'trench';     % reference system of rotation center coordinates
opt.varySub.xRot         = [0, 120];     % rotation center coordinates
opt.varySub.theta        = [10, -20];    % angles of rotation
opt.varySub.tolZ         = 1;            % tolerance when identifying the plate
opt.varySub.drawOutlines = true;         % draw outline along profile
opt.varySub.outlineProf  = [0, 0];       % coordinates of outline profile

% options to add layers
opt.varySub.addWZ        = true;         % add a weak zone
opt.varySub.d_WZ         = 20;           % thickness of weak zone
opt.varySub.ID_WZ        = 4;            % LaMEM ID
opt.varySub.type_WZ      = 0;            % LaMEM marker type
opt.varySub.d_Lith       = 100;          % thickness of overriding plate

opt.varySub.addCrust     = true;         % add crust
opt.varySub.d_OC         = 10;           % thickness of crust
opt.varySub.ID_OC        = 5;            % LaMEM ID
opt.varySub.type_OC      = 0;            % LaMEM marker type
```

Figure S2. Code snippet examples that show the options that are set in geomIO to create the geometry variations. (a) Salt diapir example. (b) Subduction example. Full codes used in this study are available on zenodo (https://doi.org/10.5281/zenodo.6538270).

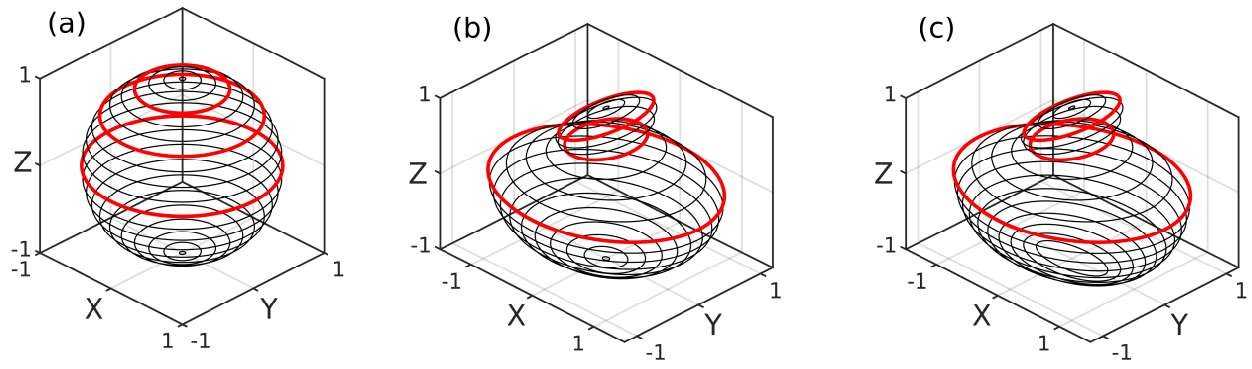

Figure S3. Illustration of 3-dimensional bodies as sets of 2-dimensional polygons. The three red polygons are the control polygons which are used to transform the body. (a) Sphere with radius 1, represented as 21 polygons. (b) Sphere from S3a after transformation by scaling. (c) Sphere from S3a with the upper half being transformed by scaling and the lower half by absolute transformation parameters. Note how the lower half is wider in S3c than in S3b.

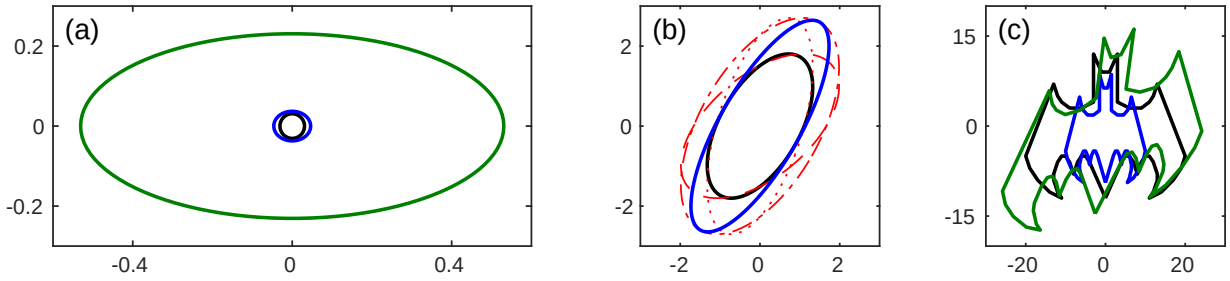

Figure S4. Illustration of how the transformation methods work on single 2-dimensional polygons. (a) Example of how the different transformation methods affect the lowermost polygon in Figure S3. Original in black, scaling in blue (used for Figure S3b) and transformation by absolute values in green (used for Figure S3c). (b) Scaling a polygon with preferred orientation. Original in black, dashed red line: Sx = 1.5, dotted red line: Sy = 1.5, dashed and dotted red line: Sx = Sy = 1.5, blue line: Sy = 1.5 and $\theta = 30$. (c) Illustration of how complex shapes are handled. Original in black, scaled version in blue (Sx = 0.5, Sy = 0.75), scaling and coordinate system rotation in green (Sy = 1.5, $\theta = 45$).

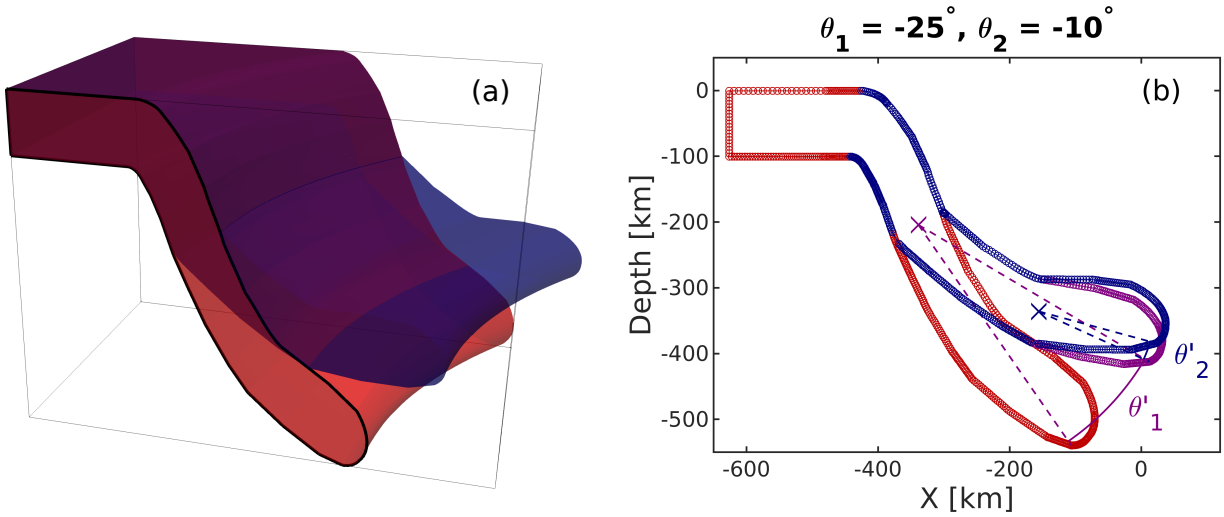

Figure S5. (a) 3D Example of a plate, subducting along a curved trench, drawn in geomIO (red) and an automatically generated variation that is bent at two locations in 200 and 320 km depth (crosses in S5b). Black line shows one of the vertical polygons that the 3D volume is represented as inside our algorithm and is identical to the red polygon in S5b. (b) Representation of the plates in S5a as vertical polygons. Red: original, purple: after the first rotation, blue: after both rotations. Crosses show the centers of rotation.

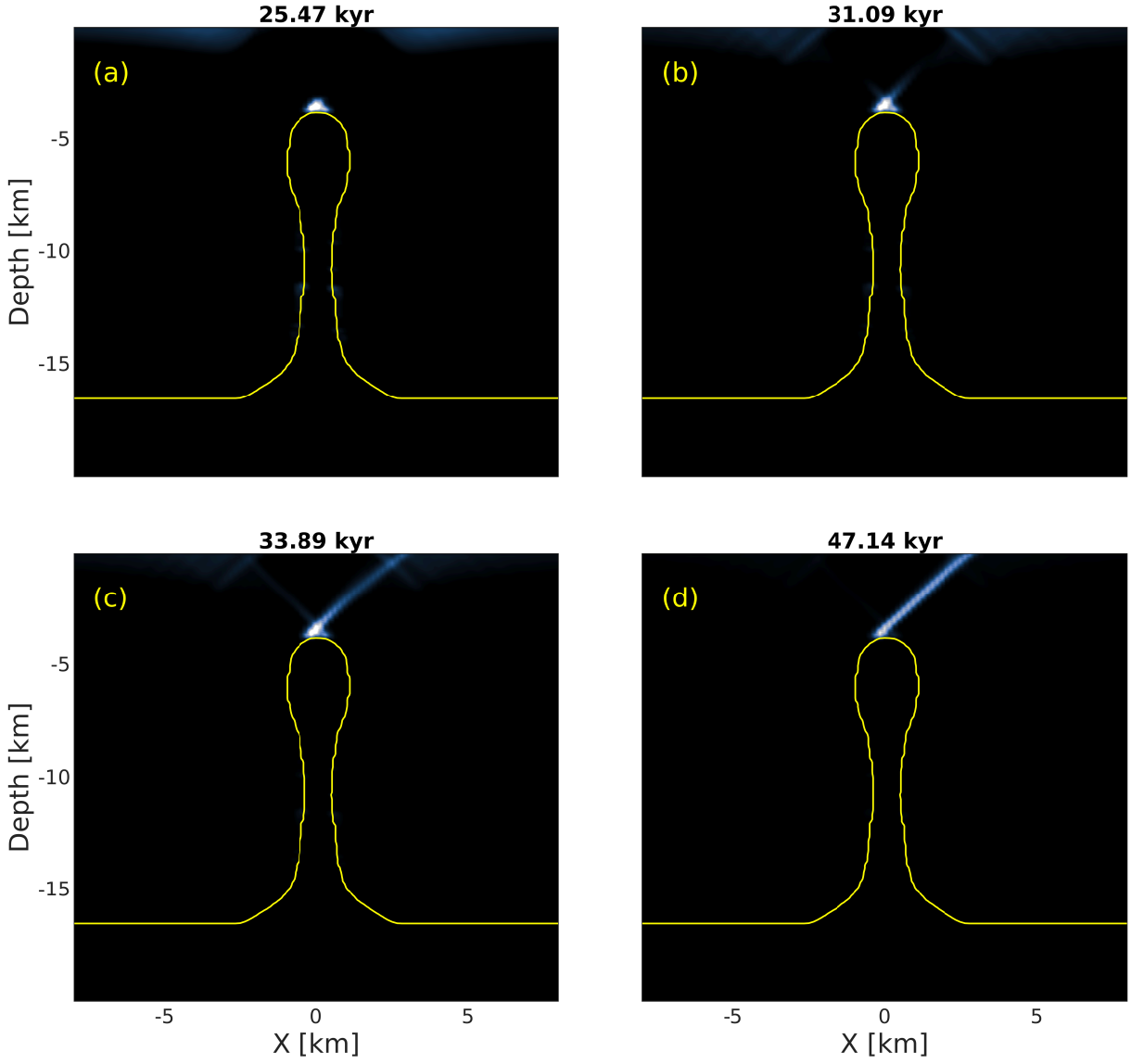

Figure S6. Evolution of plastic strain (i.e. faults) around the synthetic 'true' diapir (blue in Figure 3). (a) Early stage plastic failure along the surface and at the tip of the diapir. (b) First faults start to connect diapir and surface. (c) Faults have connected diapir and surface. Right fault takes up most of the deformation. (d) Right fault takes up all the deformation and left fault is no longer active.

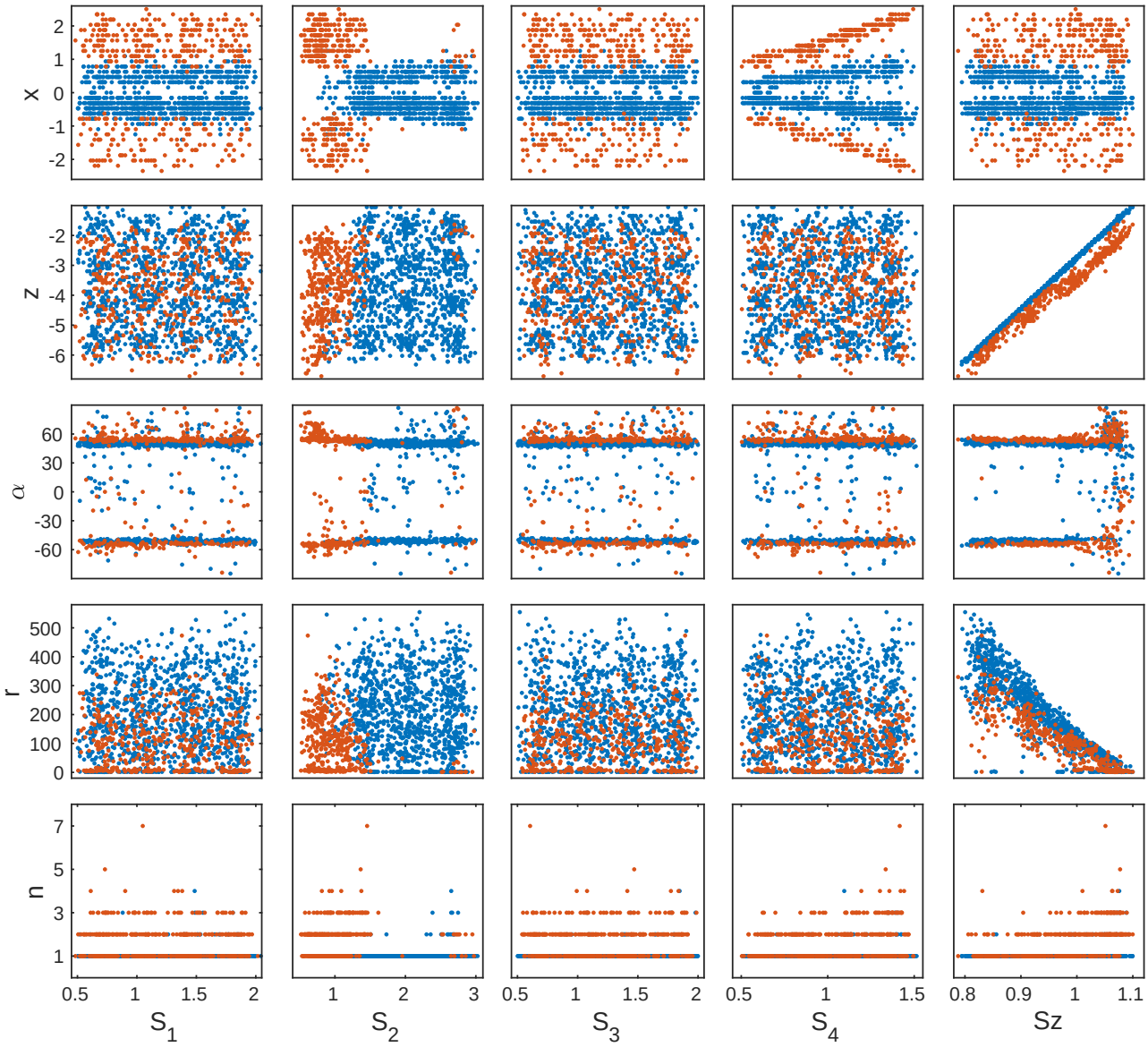

Figure S7. All fault properties in relation to each scaling parameter. x: lateral coordinate of lower fault tip, z: vertical coordinate of lower fault tip, α: dip angle of fault, r: aspect ratio of fault, n: number of faults. Blue dots denote faults that connect to the center and orange dots denote faults that connect to the side of the diapir head. Note that the orange dots are plotted on top which is why they hide a lot of blue dots in the lowest row of sub-figures.

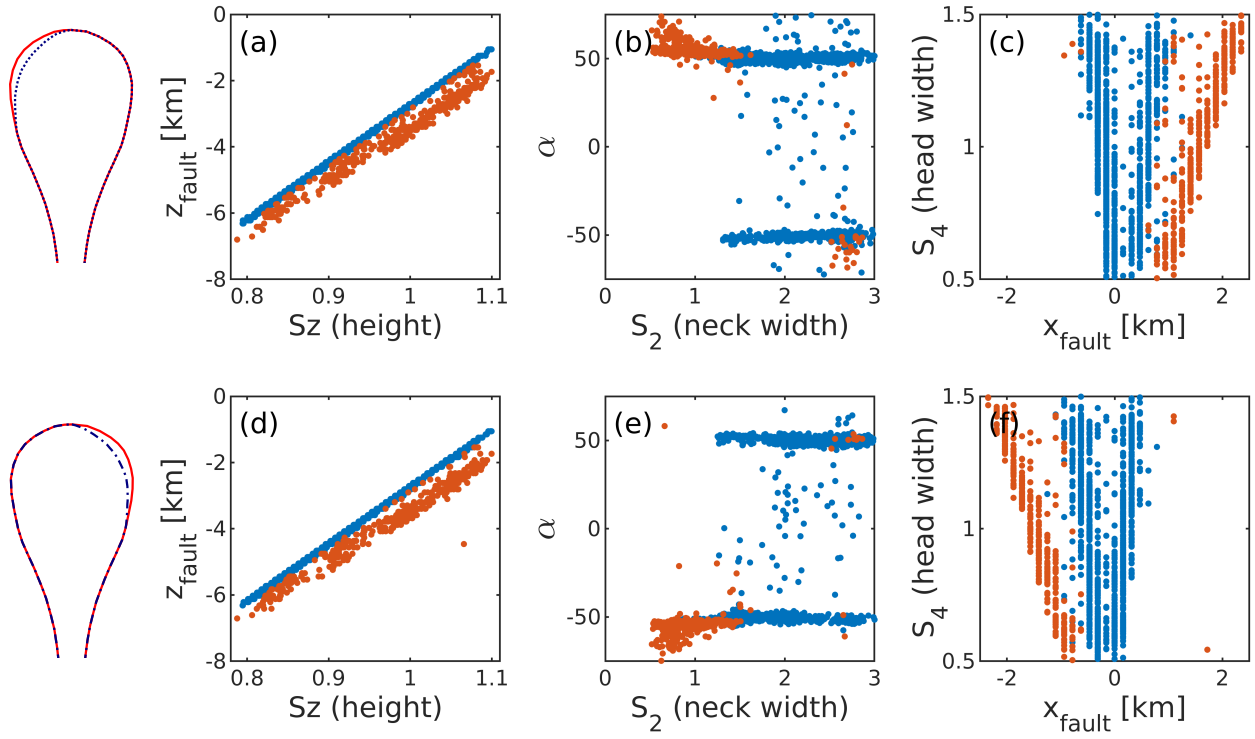

Figure S8. Results for two mirrored asymmetric setups. Upper row has been changed on the left (dotted in Figure 3), lower row on the right (dashed-dotted in Figure 3). Same color code as in Figure 5 (blue dots denote faults that developed from the center of the diapir head and orange dots denote faults that developed from it's sides). (a) and (d) Depth of the lower end of the fault in dependence of Sz. (b) and (e) Fault orientation in dependence of S_2. $\alpha < 0$: fault goes to the left. (c) and (f) Lateral position of the lower end of the fault in dependence of S_4.

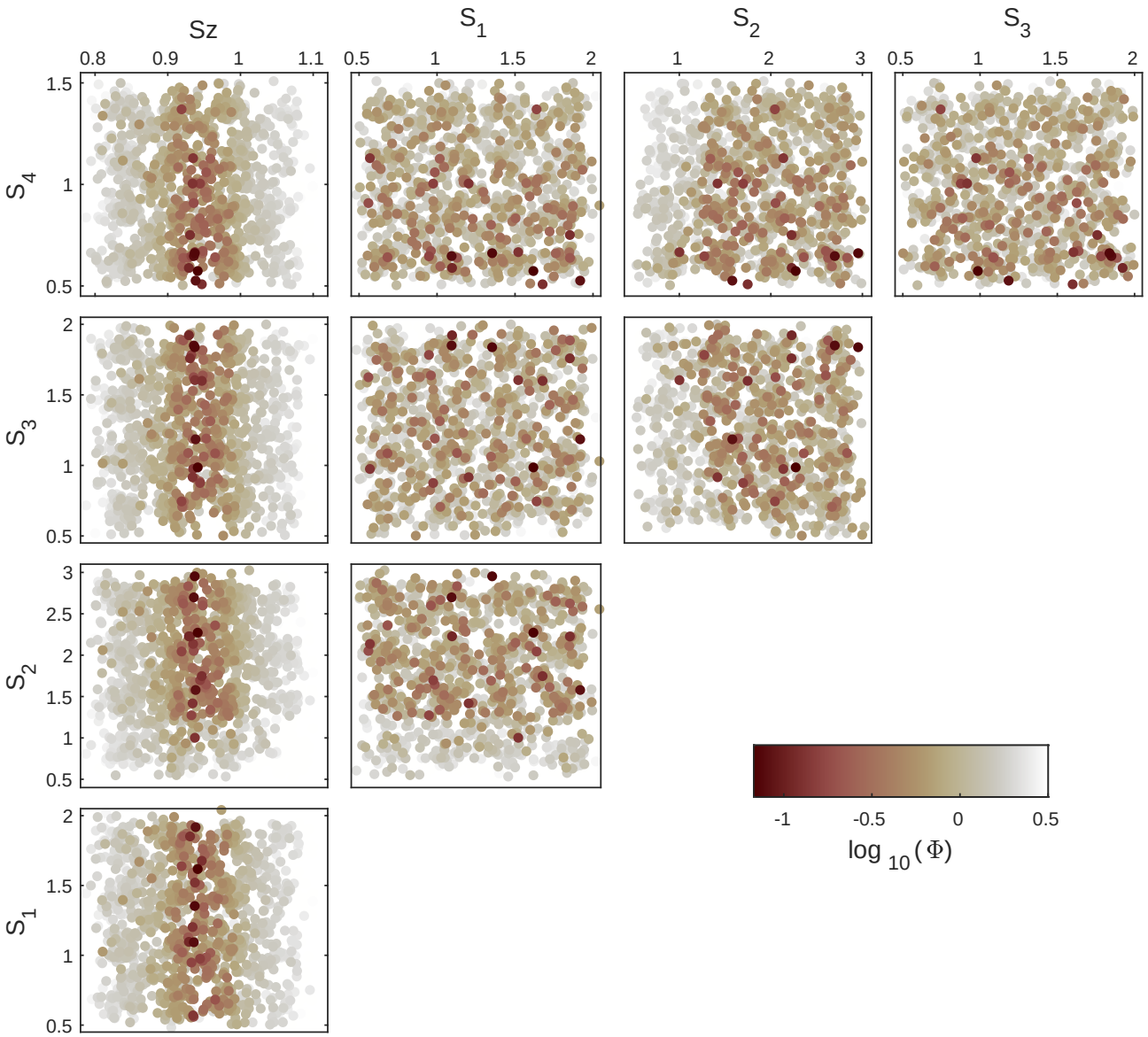

Figure S9. Misfit of the fault systems in dependence of all sets of 2 scaling parameters. Low misfit always correlates with medium Sz values and often correlates with low S_4. High misfit always correlates with low S_2. S_1 and S_3 do not show correlation with the misfit.

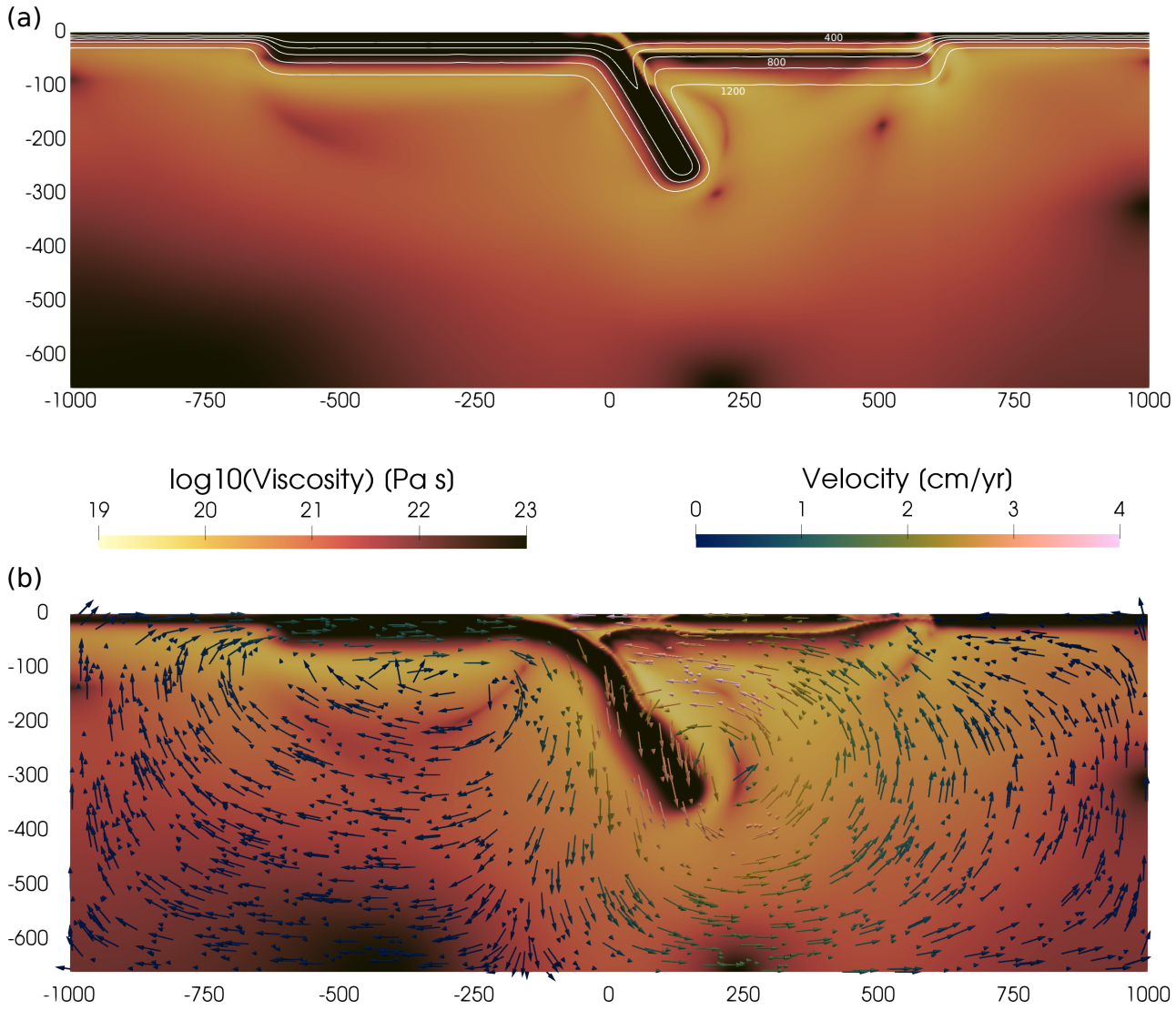

Figure S10. (a) Viscosity in the reference model ($\beta_0 = 60°$) at the first time step. White contour lines show temperature in 200 °C intervals. Top and bottom of the model have temperatures of 0 and 1350 °C respectively. Axes are in km. (b) Snapshot of the same model after 2 Myr. Slab has started to sink, trench has started retreating and continent has undergone buckling and extension. Arrows show velocity field.

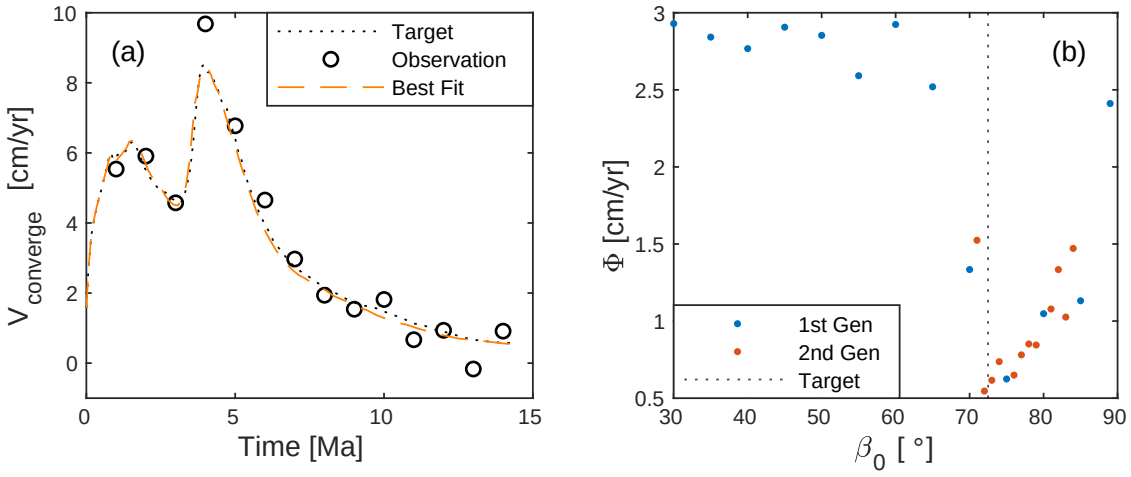

Figure S11. Results of inversion for initial angle (β_0). (a) Dotted black line shows profile of target model ($\beta_0 = 72.5°$) and black circles show noisy observation based on the target model. Dashed orange line shows best fitting model ($\beta_0 = 72°$). (b) RMS misfit (Φ) as a function of initial dip angle β_0. Blue dots shows first set of models in 5° intervals and orange dots show second set in 1° intervals in areas of low misfit. Dotted black line indicates β_0 of the target model.

Table S1. Material parameters for salt application

Material	$\rho\,[\frac{\mathrm{kg}}{\mathrm{m}^3}]$	G [GPa]	$\nu[\,]$	η [Pas]	c_0[MPa]	$\phi[^\circ]$
Crust	2700	30	0.25	10^{24}	10	30
Salt	2200	15	0.25	10^{19}	10	30

Table S2. Material parameters for subduction application

Material	$\rho\,[\frac{\mathrm{kg}}{\mathrm{m}^3}]$	$B_n\,[\mathrm{MPa}^{-\mathrm{n}}\,\mathrm{s}^{-1}]$	E_n [kJ]	$V_n\,[\frac{\mathrm{cm}^3}{\mathrm{mol}}]$	$n[\,]$	c_0[MPa]	$\phi[^\circ]$
OP* Crust	2800	6.7 x 10^{-6}	156	0	2.4	10	30
OP* Lithosphere	3250	1.1 x 10^5	530	9.5	3.5	10	30
SP* Lithosphere	3300	1.1 x 10^5	530	9.5	3.5	10	30
Mantle	3300	1.1 x 10^5	530	9.5	3.5	10	30
Weak Zone	3250	$\eta = 10^{20}$ Pas				0.1	5

*OP corresponds to overriding and SP to subducting plate.

Table S3. Scaling parameter ranges for Application I: Salt

	S_1	S_2	S_3	S_4	Sz
min	0.5	0.5	0.5	0.5	0.8
max	2.0	3.0	2.0	1.5	1.1